Simultaneous velocity and temperature measurements applied to combustion processes

Final Report

Explosion Dynamics Laboratory

California Institute of Technology

Pasadena, CA 91125 USA

Kyle Lethander

Mentors: Joseph Shepherd and Charline Fouchier

October 29, 2023

Abstract

Understanding thermal ignition is critical for improving safety and performance in aviation and process industries. However, the standard method of autoignition testing (ASTM E659) is limited to visual observation and pointwise temperature measurements. Recent work has demonstrated the promise of thermographic particle image velocimetry (TPIV) for obtaining full-field velocity and temperature measurements in high-temperature gas flows. An experiment is designed to implement this technique to study thermal ignition by seeding a test volume with BAM:Eu^{2+} phosphor particles, illuminating the flow with a combined second and fourth harmonic Nd:YAG pulsed light sheet, imaging the scattered light for PIV analysis, and detecting the luminescence intensity of two emission spectrum bands for temperature measurements. The spectral response to temperature is investigated for particles on a heated surface, and a temperature calibration using two-color thermography was successfully performed over $20-550\,^{\circ}\mathrm{C}$ using two different excitation sources. A luminescence imaging system is designed to capture 2D intensity fields of two emission bands, and a similar calibration is attempted on BAM:Eu^{2+} particles suspended in a gas flow. Challenges with the gas flow temperature calibration, such as obtaining reliable temperature ground truth of the fluid, are identified, and potential future approaches to successfully perform gas flow phosphor thermography are discussed. Lastly, a 2D surface temperature calibration was successfully performed to test the two-color thermography technique and estimate measurement errors with more accurate ground truth temperature measurements as a proof-of-concept before reapplying the technique to a gas flow.

Contents

1 Background and motivation

Characterization of combustion processes is critical for ensuring safety and optimizing performance in aviation and process industries. One phenomenon of particular importance is autoignition of hydrocarbon fuels at relatively low temperatures and standard atmospheric pressure due to its relevance for mitigating explosion hazards on aircraft. The standard method of autoignition testing, ASTM E659, describes one process for determining chemical autoignition temperatures [1], and the results continue to serve as industry-accepted values for aircraft certification. The test has been extensively applied at the Caltech Explosion Dynamics Laboratory (EDL) to examine ignition of aviation kerosene (Jet A) and fuel surrogates [2]. However, the approach is limited to visual analysis of flame luminosity and pointwise thermocouple measurements because there is no direct optical access to the test section on the current test setup (Figure 1).

The processes involved in autoignition are not fully understood, so full-field velocity and temperature measurements would provide valuable information to study the flow dynamics preceding thermal ignition. The present work aims to apply recent developments in phosphor thermography and particle image velocimetry (PIV) to non-invasively measure velocity and temperature in autoignition experiments. First, we successfully apply PIV to decaying and forced convection flows of phosphor particles suspended in an air

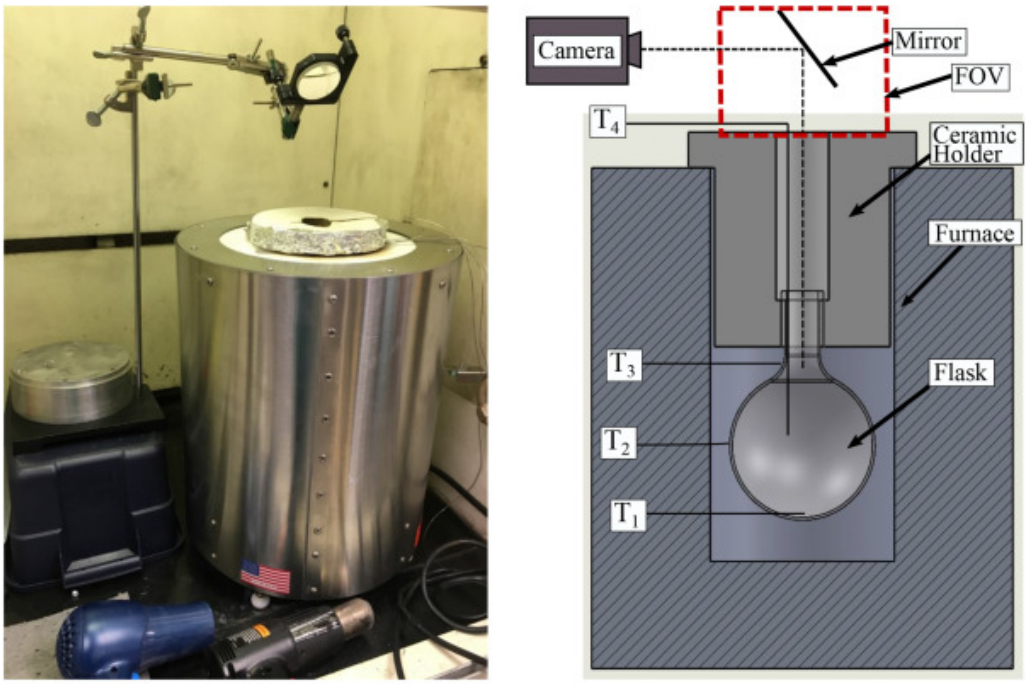

Figure 1: (a) ASTM E659 test setup used for autoignition experiments with Jet A and fuel surrogates and (b) cross section schematic [2].

volume. Next, we demonstrate the principle of phosphor thermography through multiple surface temperature calibrations and by computing the 95% confidence interval width for out-of-sample measurements over the temperature range $20 - 550\,^{\circ}\mathrm{C}$ to evaluate the associated uncertainty. The sensitivity of the temperature calibration curve to excitation spectrum is analyzed, illustrating the importance of matching the excitation source used in calibration and experiment. Finally, in-situ gas flow temperature calibrations reveal several challenges with implementing the technique with particles suspended in a fluid, such as calibration temperature measurement reliability, low filtered luminescence intensities, and image alignment in post-processing.

The remainder of this report is organized as follows. Section 2 describes the operating principle of PIV and two-color phosphor thermography. Section 3 summarizes the experimental setup designed to acquire scattering and luminescence images of particles suspended in an air volume for post-processing into temperature and velocity fields. Section 4 summarizes progress on velocity field measurements and both surface and gas flow temperature calibration attempts. The progress and challenges encountered in this investigation and directions for future work are discussed in Section 5.

2 Methods

2.1 Particle image velocimetry

Digital PIV is a popular approach for performing relatively noninvasive, full-field and time-resolved velocity measurements in liquid and gas flows [3]. The technique involves seeding a flow with micron-sized tracer particles (e.g., oil or TiO_2) that are assumed to travel with the local fluid velocity. The validity of this assumption is determined by the

Stokes number

$$\mathrm{Stk} = \frac{\tau_v u_0}{l_0}, \tag{1}$$

which describes the ratio of characteristic particle kinematic relaxation time τ_v to characteristic flow time l_0/u_0. For a uniform-density sphere, the Stokes flow approximation ($\mathrm{Re}_d << 1$) gives the kinematic relaxation time constant due to a step change in flow velocity,

$$\tau_v = \frac{\rho_p d_p^2}{18\mu_s} \tag{2}$$

for particle density ρ_p, particle diameter d_p, and fluid dynamic shear viscosity μ_s. This is a crude approximation of true particle geometries (Figure 2), but the spherical assumption is conservative because any other volume-equivalent object will only equilibrate with local flow changes in less time. The condition of strong particle adherence to the local flow velocity is $\mathrm{Stk} << 1$. For $\mathrm{Stk} < 0.1$, it can be shown that the tracking error is less than 1% [4].

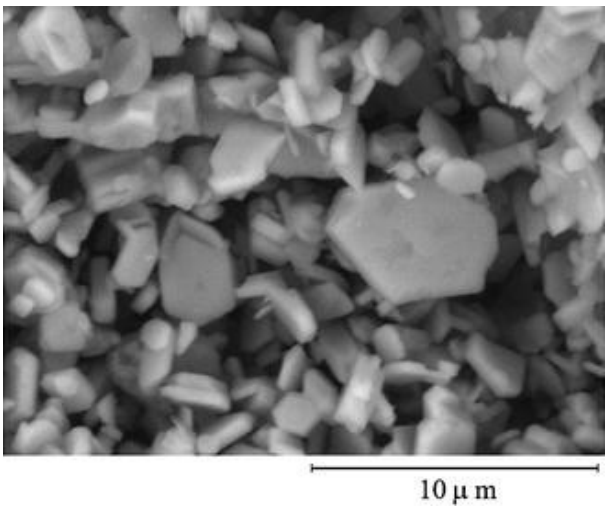

Figure 2: Scanning electron microscope image of BAM:Eu^{2+} phosphor particles (Phosphor Technology, Ltd.).

A dual-cavity, second harmonic Nd:YAG laser is used to illuminate the seeding particles twice in rapid succession using a series of lenses to expand the beam into a thin light sheet inside the test volume. A properly formed light sheet reaches a thickness minimum, or waist, at the test section, enabling the in-plane motion of particle ensembles to be visualized over a small inter-frame time Δt. At each sample time, two frames are recorded using a high-speed camera (Figure 3).

The time Δt is tuned to achieve the desired particle displacement between frames in each image pair. Each frame is divided into square interrogation windows sized such that particle displacements are no more than $\sim 1/4$ of the initial interrogation window size. Local displacements throughout the field can be computed using a variety of algorithms, such as direct cross correlation but more commonly direct Fourier transform correlation using multiple passes with shrinking and deforming interrogation windows [5, 6]. A calibration distance is applied to convert pixel displacements to length displacements, from which the velocity field is computed using the inter-frame time Δt. For time interval T between image pairs, the full velocity field is obtained at a sample frequency $f_s = 1/T$. The timing diagram for two cycles of laser pulses and PIV camera exposures of duration

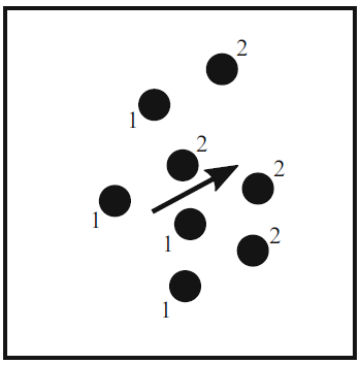

Figure 3: Schematic illustrating the shift in a particle ensemble from t_1 to $t_2 = t_1 + \Delta t$ used to perform PIV analysis (reproduced from [3]).

$t_{e,1}$ is provided to illustrate the image pair capture scheme (Figure 4, top and middle). The vector field in Figure 5 is the final result of PIV applied to flow over a heated cylinder with a sample frequency $f_s = 200\,\text{Hz}$.

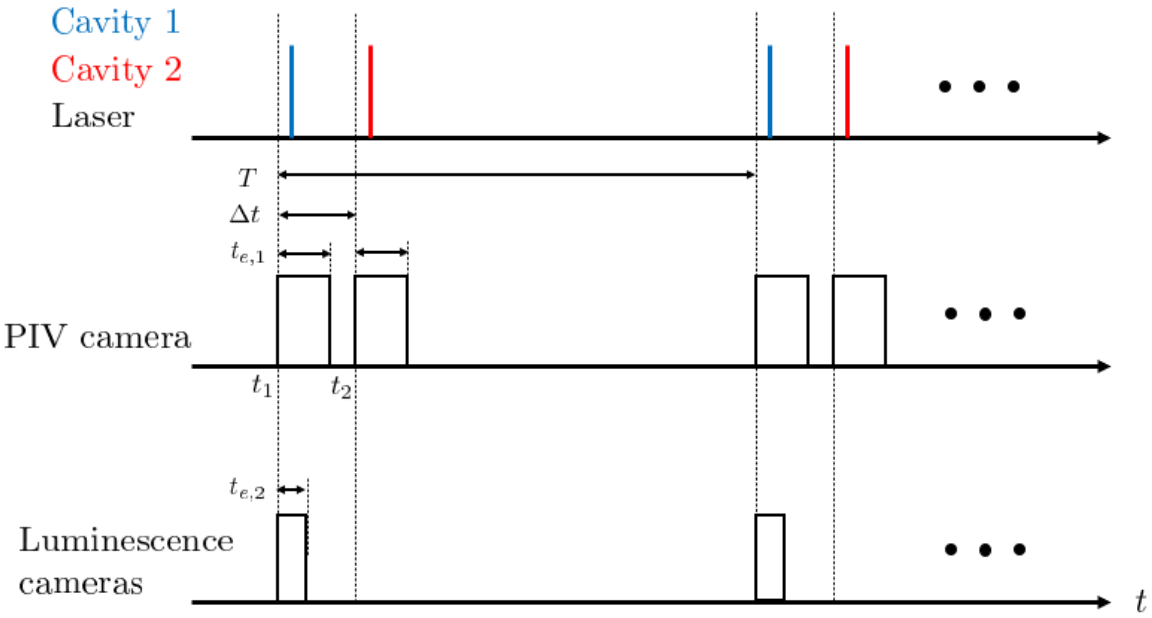

Figure 4: Laser and camera timing diagram for recording image pairs with inter-frame time Δt, sample frequency $1/T$, PIV camera exposure $t_{e,1}$, and luminescence camera exposure $t_{e,2}$.

Many PIV codes have been developed and verified for processing raw frames into velocity fields. In this work, the MATLAB implementation of PIVlab [5, 6, 7] is used due to its widespread use in the PIV community, extensive testing, and simple user interface.

2.2 Two-color phosphor thermography

Phosphor thermography is a powerful technique for high spatial resolution surface and fluid flow temperature measurements [8]. It has been combined with PIV to study turbulent combustion in internal combustion engines [9], falling droplets of diluted iso-octane

[10], shear layers [11], fuel sprays [12], heated air jets [13], and cylinder wakes [14], among other applications. The capability of gas flow phosphor thermography is illustrated by temperature fields measured from experiments of flow over a horizontal heated cylinder [14] (Figure 5).

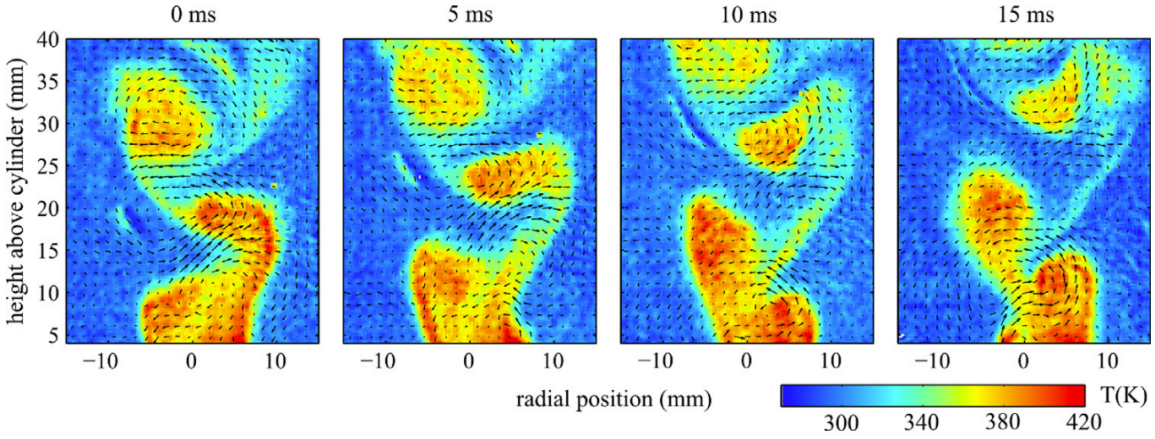

Figure 5: Time evolution of the combined velocity and temperature field over a heated cylinder computed using TPIV (reproduced from [14]).

The operating principle of two-color phosphor thermography is the temperature sensitivity of the phosphor emission spectrum (Figure 6, left). The integrated intensity of phosphor emission over a limited range of wavelengths depends on the local seeding density N_p, the filter transmission function $\tau(\lambda)$, the total emission intensity temperature dependence $Q(T)$, and the local laser fluence $S(F)$, where $F = F(x, y, t)$. To summarize, the intensity of emission band i scales according to [15]

$$I_i \propto N_p,\ \int_0^\infty E(\lambda, T)\tau_i(\lambda)\, d\lambda,\ Q(T),\ S(F) \tag{3}$$

where $E(\lambda, T)$ is the spectral radiance. Two emission bands can be measured to tabulate an emission intensity ratio as a function of temperature (Figure 6, right). The advantage of calibrating the intensity ratio, rather than absolute intensity, as a function of temperature is to eliminate all dependencies except the emission spectrum temperature dependence,

$$\varphi(T) = \frac{I_B}{I_A} = \frac{\int_0^\infty E(\lambda, T)\tau_B(\lambda)\, d\lambda}{\int_0^\infty E(\lambda, T)\tau_A(\lambda)\, d\lambda} \tag{4}$$

and thus the measured value φ is theoretically only a function of temperature. The phosphor host crystal, dopant ions, and bandpass filters should be selected to maximize the fractional sensitivity of φ and total intensity measured by the detector (e.g., a CCD camera sensor) while minimizing spatial and temporal intensity variance.

Similar to PIV, phosphor thermography relies on measuring a property of the phosphor particles to indirectly infer the associated property in the fluid. The characteristic thermal particle response time to a step change in temperature is given by

$$\tau_T = \frac{\rho_p C_p d_p^2}{12 k_{\text{air}}}, \tag{5}$$

where C_p is the particle specific heat capacity and k_{air} is the fluid thermal conductivity. Equation 5 can be used to compute a thermal Stokes number (Equation 1) to ensure the

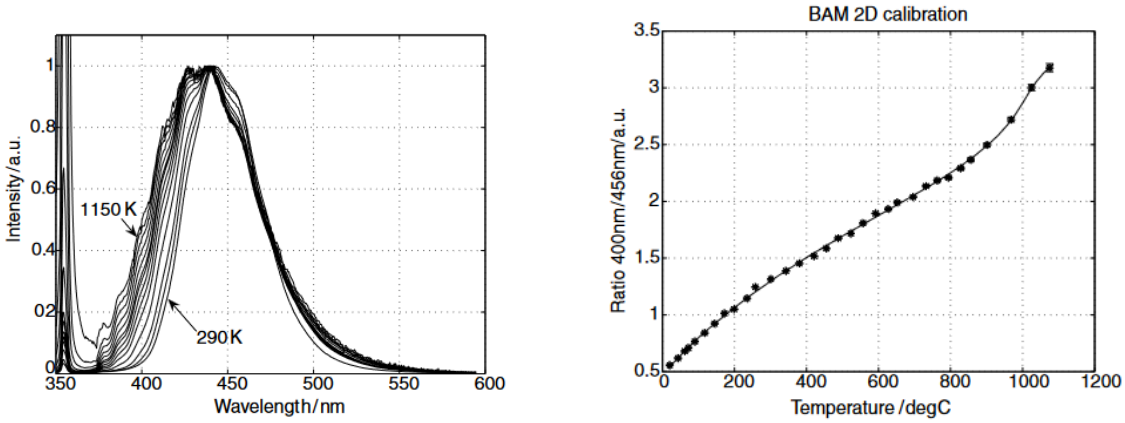

Figure 6: BAM:Eu^{2+} emission spectrum due to 355 nm excitation (left) and luminescence intensity ratio calibration curve (right) (reproduced from [16]).

characteristic flow time is much larger than the time required for particles to equilibrate with the local temperature.

Full-field intensity of two emission bands can be obtained by adding two cameras equipped with interference filters opposite the high-speed camera for PIV (Figure 7). A beamsplitter is positioned in front of the luminescence cameras, oriented perpendicular to one another to capture the red and blue ranges of the phosphor emission, respectively. Unlike PIV, phosphor thermography does not require cross-correlation, so a single exposure of duration $t_{e,2}$ to capture the first laser pulse is sufficient at each sample time (Figure 4, bottom). The exposure can also be set to capture both laser pulses should higher luminescence intensity be desired. A setup similar to Figure 7 has been designed with an optically accessible test section to perform spatially and temporally resolved temperature and velocity measurements in a gas flow.

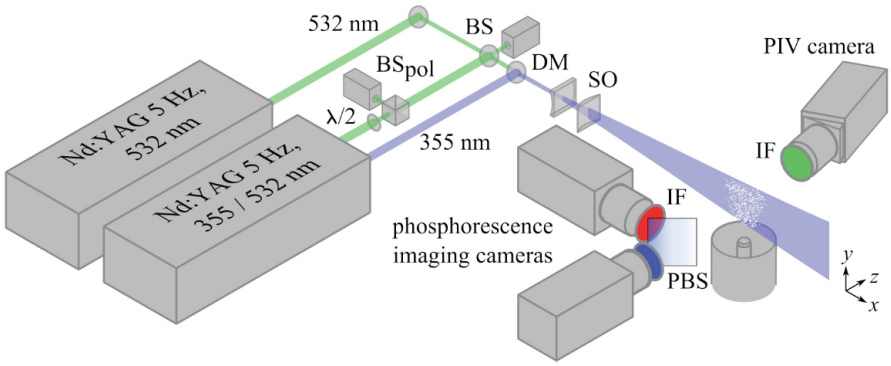

Figure 7: Experimental setup for TPIV, including lasers, sheet optics, and cameras equipped with interference filters to acquire scattering and luminescence intensities (reproduced from [17]).

3 Experimental design

3.1 Phosphor particle selection

The choice of phosphor host crystal, dopant ions, and ion concentration is critical to minimize uncertainty in the measured temperature. A literature review was conducted to survey phosphors previously used for gas flow phosphor thermography. Several important properties of each phosphor are reported (Table 1): the optimal operating temperature range T_{op}, excitation wavelength λ_{ex}, and emission lifetime τ_{em}. The emission lifetimes are given for the lower range of operating temperatures and decrease with the onset of thermal quenching as temperature is increased.

Phosphor	T_{op} (K)	λ_{ex} (nm)	τ_{em} (μs)	References
Eu:BAM	300–1000	266, 355	1	[18, 17, 16, 19, 20, 21, 15, 22, 23, 24, 25]
Pr:YAG	500–800	266	0.06	[23, 26, 27, 28, 29]
Ce:LuAG	600–900	355	0.06	[22, 23, 27, 30]
Ce,Pr:YAG	300–500	266	0.06	[31, 32]
Ce,Pr:LuAG	400–1000	266	0.06	[22, 31, 33, 34]
Ce:$GdPO_4$	400–1200	266	0.031	[22, 23, 33, 35]
Ce:CSSO	400–1400	266	0.075	[33, 36]
Ce,Pr:CSSO	300–925	266	0.027	[22, 36]
Zn:ZnO	300–500	355	< 0.001	[16, 37]

Table 1: Excitation and emission properties for some phosphors used for gas flow phosphor thermography.

The most important phosphor selection criterion is the operating temperature range, loosely defined as the set of temperatures where measured temperature uncertainty is bounded by some prescribed value (e.g., $\sigma_T < 30\,\mathrm{K}$) [23]. The fractional sensitivity of intensity ratio is given by

$$\zeta = \frac{1}{\varphi}\frac{d\varphi}{dT} = \frac{d}{dT}(\log\varphi) \tag{6}$$

and is used to compute a theoretical temperature measurement standard deviation

$$\sigma_T = \zeta^{-1}\eta \tag{7}$$

where

$$\eta = \sqrt{\left(\frac{\sigma_{I_A}}{I_A}\right)^2 + \left(\frac{\sigma_{I_B}}{I_B}\right)^2} \tag{8}$$

represents the normalized intensity ratio uncertainty due to variance in measured intensities of each emission band. As shown by Equations 6–8, temperature variance is minimized by selecting a phosphor with high temperature sensitivity and emission intensity and using a detector with low shot-to-shot variance in measured intensity for constant

incident intensity. These requirements are accomplished by selecting a phosphor with significant spectral shift over the target temperature range, choosing wide bandpass filters, one of which increases the integrated intensity with temperature and the other which is invariant (or decreases) with temperature, and detecting the emission intensity using a sensor with high signal-to-noise ratio.

Based on temperature traces collected from previous autoignition experiments [2], the target temperature range for this investigation is 400–850 K. For this work, we chose the phosphor BAM:Eu^{2+}, which has been studied extensively for flow thermometry due to its high quenching temperature, broadband excitation spectrum, and reasonably large operating temperature range. It is a suitable phosphor for simultaneous velocity measurements because it emits in the blue region, which prevents interference with 532 nm light scattered for measurements using a conventional PIV setup. Additionally, its absorption spectrum allows for excitation by either 355 nm or 266 nm (Figure 8), which was an important consideration for this project because multiple excitation sources were applied for various surface and gas flow temperature calibration attempts.

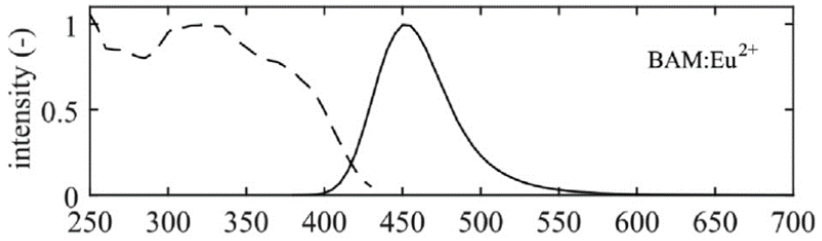

Figure 8: Excitation (dotted line) and emission (solid line) spectra of BAM:Eu^{2+} at room temperature (reproduced from [38]).

As described in Section 2, the measurement techniques employed for this project directly measure properties of the phosphor tracer particles to infer the associated property in the fluid. Consequently, it is critical to ensure the seed particles faithfully track both the local velocity and temperature of the flow. The characteristic kinematic time constant using room temperature properties of air and approximate thermal and mechanical properties of BAM:Eu^{2+} was found to be $\tau_v \approx 46\,\mu$s, and the characteristic thermal relaxation time was computed to be $\tau_T \approx 40\,\mu$s. Both characteristic times are orders of magnitude smaller than the maximum expected flow timescale, which validates the assumption of local equilibrium with the flow.

3.2 Light generation

The experimental setup consists of a light generation system, a test section, and a scattering and luminescence detection system (Figure 9).

A second harmonic generator (SHG) and sheet-forming lens system (Figure 10) were designed to generate sheets of light containing second and fourth harmonics of the Nd:YAG lasing medium (532 and 266 nm) for scattering and particle excitation, respectively. The output of a dual-cavity second harmonic Nd:YAG laser (Quantel EverGreen model EVG00070) was processed by a half-wave plate (Thorlabs WPH05M-532) to rotate the linear polarization of the light before entering a high-power polarizing beamsplitter (Thorlabs PBS25-532-HP).

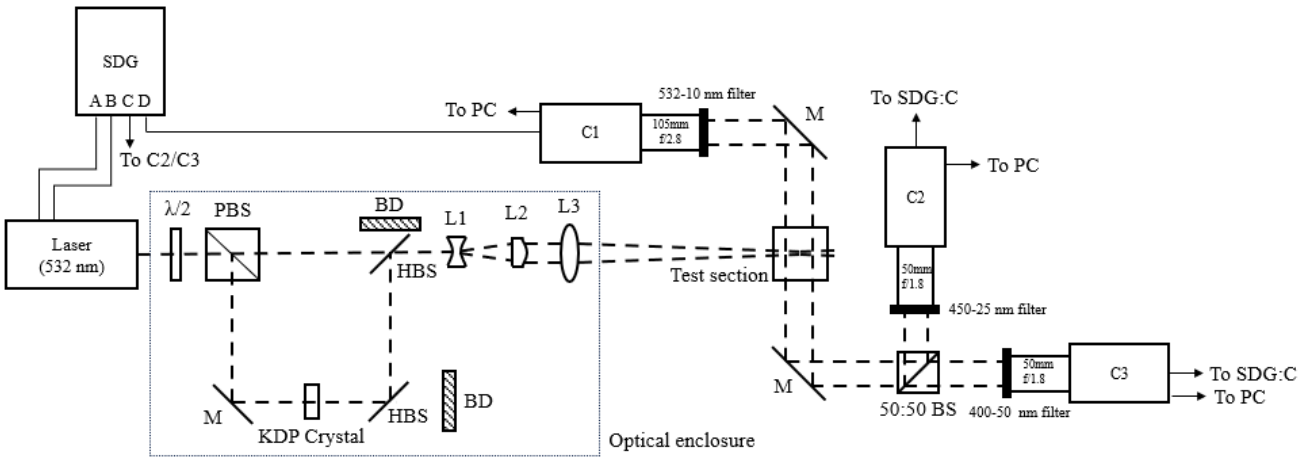

Figure 9: Experimental setup (top view) for second harmonic generation, sheet-forming, and imaging of particle scattering and emission. $\lambda/2$: half-wave plate, PBS: polarizing beamsplitter, HBS: harmonic beamsplitter, BS: beamsplitter, L: lens, C: camera, M: mirror, SDG: signal delay generator, BD: beam dump.

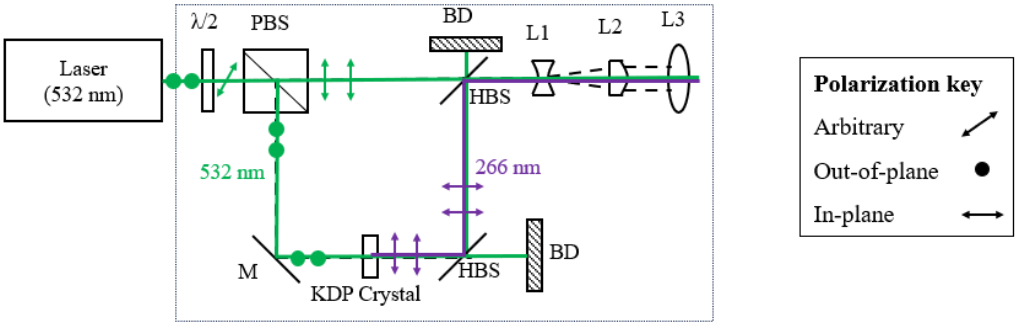

Figure 10: Schematic of the SHG and sheet-forming lenses used to produce a combined 532/266 nm light sheet.

The p-polarized component of the beam was transmitted through the polarizing beamsplitter while the s-polarized component was reflected. The transmitted component passed through a harmonic beamsplitter (Thorlabs HBSY134) before entering the sheet-forming optics (L1, L2, and L3), and the reflected component was guided by a high-power mirror (Thorlabs NB1-K12) through a nonlinear crystal (Edmund Optics #24-197) mounted on a precision rotation mount inside a cage cube for fine angular adjustment. A harmonic beamsplitter placed after the crystal reflected the fourth harmonic while transmitting and discarding excess second harmonic light. A second harmonic beamsplitter (Thorlabs HBSY134) was used to recombine the second and fourth harmonic beams before sending both through the sheet-forming optics.

UV fused silica AR-coated lenses were used to expand the beam into a thin sheet of light inside the test section. The lens types and focal lengths for lens 1 (L1), lens 2 (L2), and lens 3 (L3) are given by, respectively, a bi-concave spherical lens ($f_1 = -50\,\text{mm}$), a plano-convex cylindrical lens ($f_2 = +100\,\text{mm}$), and a bi-convex spherical lens ($f_3 = +500\,\text{mm}$). A 2D ray-tracing program was written to compute the laser sheet height at the waist (Figure 11).

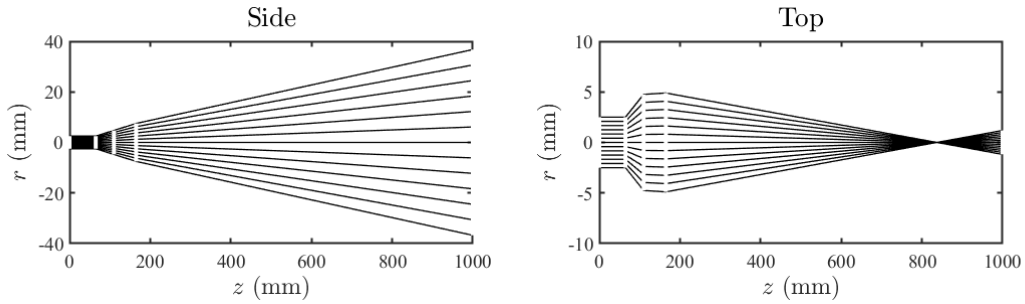

Figure 11: Side and top views of the laser sheet profile calculated using 2D ray-tracing with the small angle approximation.

3.3 Test section and particle seeding

A test section (10 cm × 10 cm × 10 cm) was designed to contain the particles suspended in a heated mixture. The system was fabricated using a copper base plate with vertical extruded metal standoffs with channels to accept transparent windows, two of which were chosen to be quartz to transmit UV light. A stainless-steel sheet was placed atop the metal standoffs to prevent particle leakage while remaining open to the atmosphere. Holes were drilled in the sheet to accept a segment of copper tubing (to be discussed) and a thermocouple.

Preliminary experiments to test solid particle suspension using the fan from oil particle PIV experiments proved this approach would not work due to particle agglomeration and sticking to the test section walls. A simple seeding mechanism was implemented by impulsively forcing the particles with a short blast of air (Figure 12).

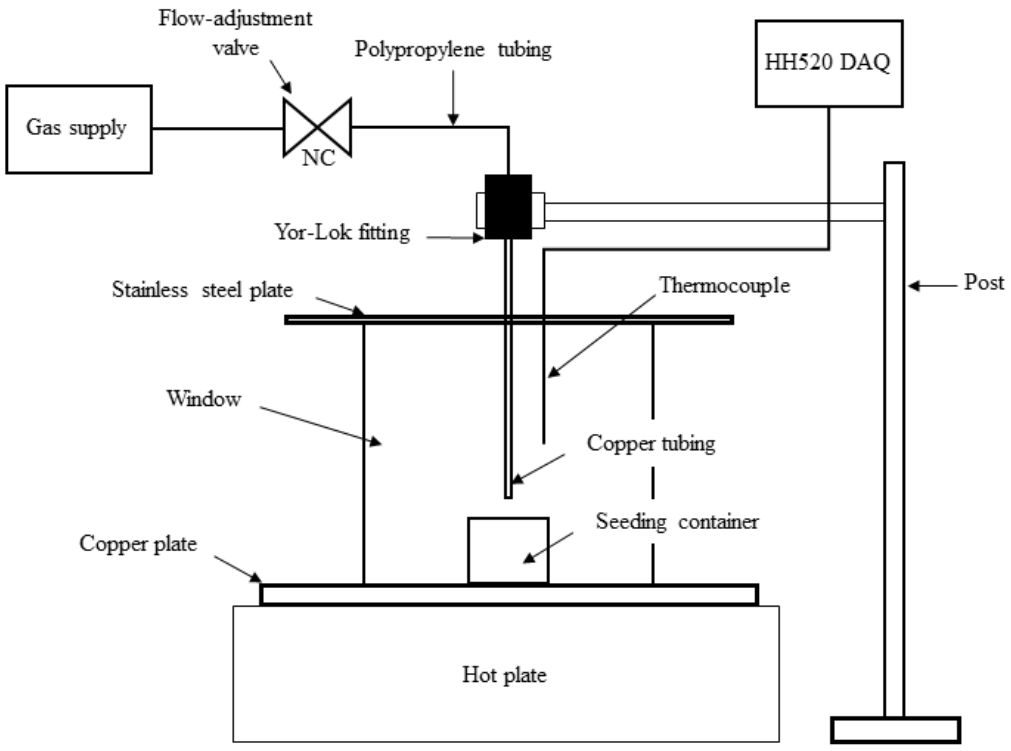

Figure 12: Test section and seeding mechanism for suspending tracer particles inside an enclosed air volume.

A compressed air supply was connected to a normally closed valve and fitted to a piece of copper tubing (⌀1/16 in) positioned inside the test section through a hole in the stainless-steel cover. A flow-adjustment valve was added downstream to modulate the flow rate. A tube cap was fixed to the copper base plate and used to contain the particles prior to suspension. The test section was heated using a hot plate capable of reaching surface temperatures up to $\sim 625\,^{\circ}\mathrm{C}$. To provide the temperature associated with calibration data, a thermocouple was suspended inside the test volume away from the copper tubing (Figure 21).

3.4 Scattering and luminescence detection

An imaging system was required to measure scattered light and luminescence intensity of the seeded phosphor particles. The setup used for this project consisted of a Vision Research Phantom v710 high-speed camera (C1) and two PCO 2000 monochrome CCD cameras (C2, C3) (Figure 13). The high-speed camera was equipped with a 105-mm lens (Nikon AF Micro-NIKKOR, 105mm f/2.8), and 50-mm lenses (Nikon AF NIKKOR, 50mm f/1.8) were attached to the two CCD cameras. A 50:50 beamsplitter cube (Thorlabs BS031) was used to divide light between the CCD cameras to capture full images of two emission bands. A 532-10 nm bandpass filter (Edmund Optics #65-216) was placed in front of C1 to measure scattered light for PIV analysis and an angled 515 nm longpass colored glass filter (Edmund Optics #14-495) to prevent reflected luminescence from interfering with the phosphor emission images. The first luminescence camera (C2) detected the long wavelengths of the emission spectrum using a 450-25 nm filter (Edmund Optics #86-665), and the second luminescence camera (C3) detected the short wavelengths using either a 400-50 nm or 425-50 nm filter (Edmund Optics #84-793 and #86-961, respectively).

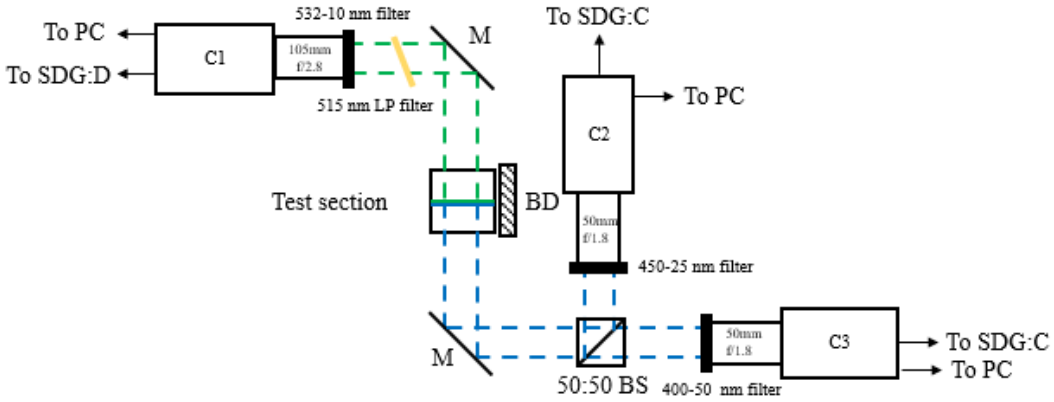

Figure 13: Scattering and luminescence imaging systems for PIV and phosphor thermography, respectively.

The pulsed laser and all cameras C1, C2, and C3 were synchronized to an internally triggered signal delay generator (Berkeley Nucleonics Series 575).

3.5 Phosphor surface spectroscopy

To test the emission spectrum response to temperature changes prior to attempting a gas flow calibration, surface spectra were recorded using a continuous wave broadband

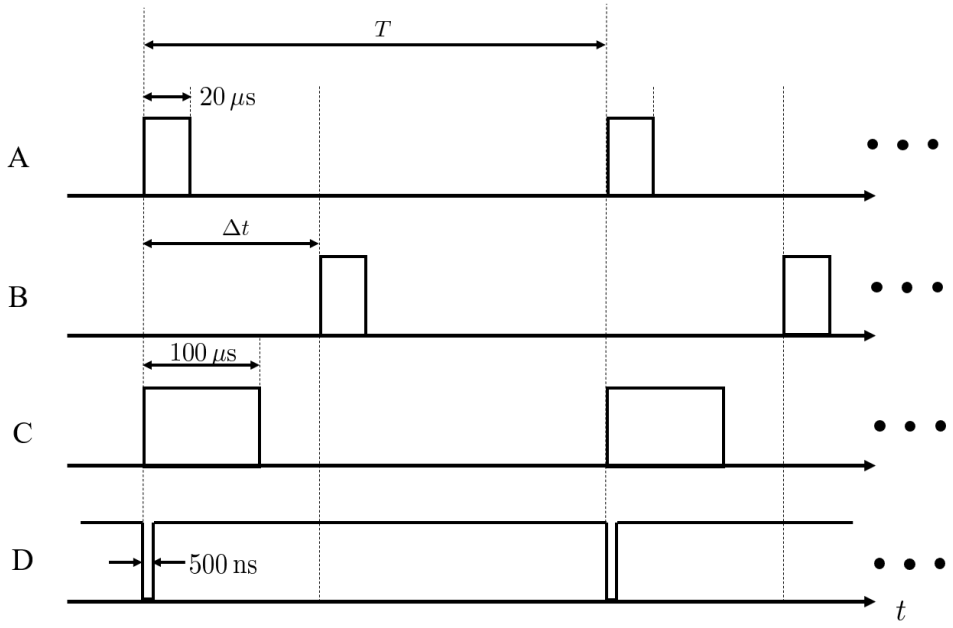

Figure 14: Signal delay generator timing diagram. Outputs are connected to (A) laser cavity 1, (B) laser cavity 2, (C) PCO 2000 CCD cameras, and (D) Phantom v710 high-speed camera.

UV excitation source. Bulk powder BAM:Eu^{2+} was placed on a horizontal stainless-steel sheet and rested on a hot plate. The output of a laser-driven light source (LDLS) (Energetiq Model EQ-99X-FC) was passed through a filter (SCHOTT UG11, Edmund Optics #84-899) to extract only UV wavelengths from the broadband output (Figure 15). A focusing lens connected to a spectrometer (Ocean FX Miniature Spectrometer) was directed toward the pile of phosphor powder and used to measure luminescence intensity versus wavelength.

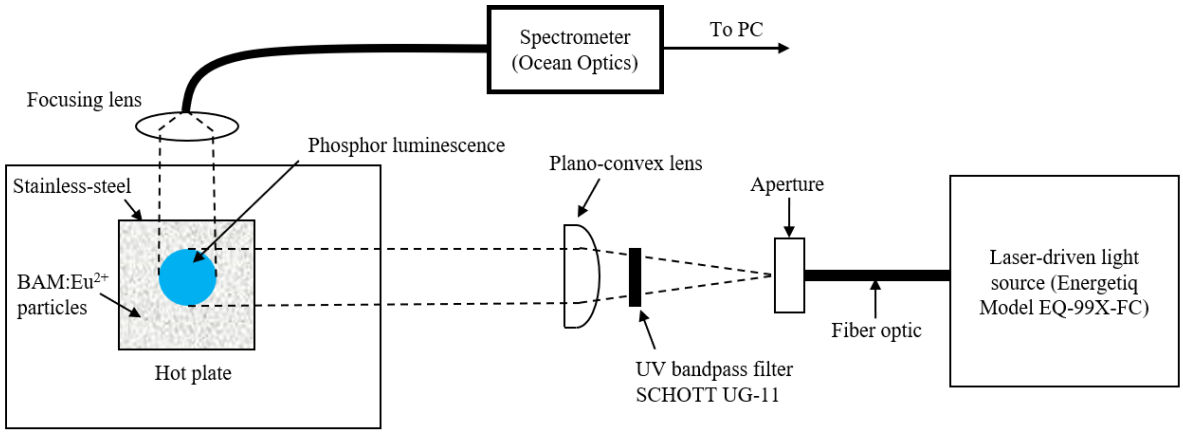

Figure 15: Surface temperature calibration setup (top view) using broadband UV excitation and phosphor emission measurements using a spectrometer.

4 Results

4.1 PIV with BAM:Eu^{2+}

The test section and seeding mechanism were tested by performing PIV experiments of decaying and forced convection flows using BAM:Eu^{2+} seed particles. The test volume was seeded with $< 5\,\text{mg}$ phosphor powder, but the exact quantity was below the precision of the digital balance and thus could not be measured. Several tests were executed using various impulse intensities achieved using a flow-adjustment valve to change the upstream pressure in the tube. Preliminary investigations were performed to determine the magnification required to resolve light scattered off the BAM:Eu^{2+} particles over multiple pixels, which was found to be critical for successful PIV analysis. The field-of-view (FOV) was measured using a dotted calibration target and found to be $1.18\,\text{in} \times 0.89\,\text{in}$. Image pairs were collected at the maximum laser repetition rate, $f_s = 15\,\text{Hz}$ and an inter-frame time $\Delta t = 620\,\mu\text{s}$. Manual validation was applied by rejecting vectors outside half the maximum interrogation window size. A parametric study was performed to analyze the sensitivity of calculated displacement fields on image preprocessing, and no significant difference was observed. Example displacement component fields (horizontal and vertical components u and v, respectively) are provided to illustrate the post-processed result prior to length scale calibration and division by Δt (Figure 16).

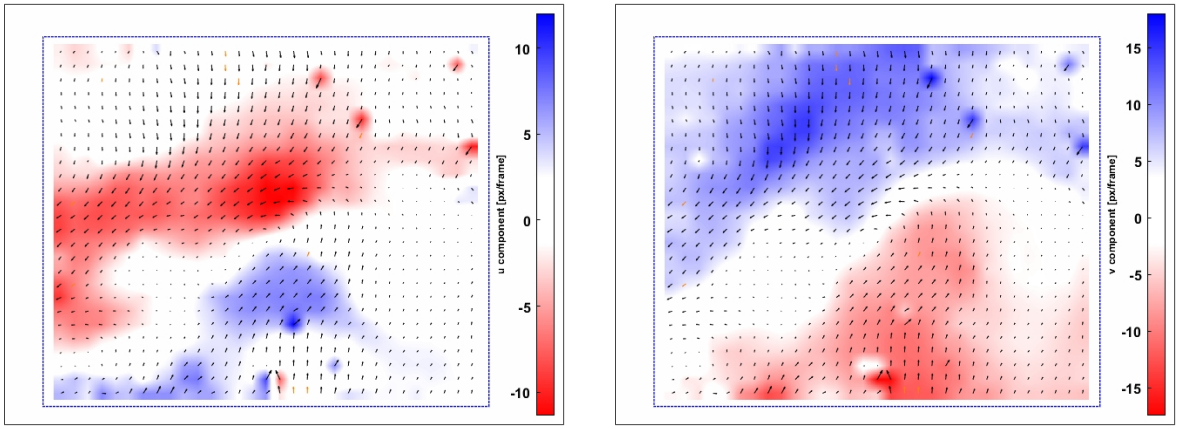

Figure 16: Example of post-processed pixel displacement field (left: u, right: v) from data collected by the PIV system with BAM:Eu^{2+} tracer particles.

This investigation confirmed successful particle suspension using the proposed seeding approach and verified the feasibility of obtaining sufficient scattering intensity for running the PIV algorithm. However, there is a fundamental limitation on the maximum FOV possible for a given camera sensor pixel array and particle size distribution. Several Nikon lenses with various focal lengths were tested to maximize the FOV without leading to a significant number of spurious vectors in the post-processed results from PIVlab. The FOV reported above ($1.18\,\text{in} \times 0.89\,\text{in}$) was nearly the maximum achievable in this study, which is quite small compared to the overall test volume size. This will need to be considered for future experiments where a larger FOV is desired, especially for overlapping the results with calculated temperature fields.

4.2 Surface phosphor thermography

4.2.1 Broadband UV excitation

BAM:Eu^{2+} particles were first applied to a sheet of borosilicate glass, and the emission following broadband UV excitation by the LDLS was visualized to verify sufficient luminescence for phosphor thermography (Figure 17).

Figure 17: Surface adhesion and emission of BAM:Eu^{2+} particles captured on a smartphone camera.

Due to the low thermal conductivity of glass and the difficulty of fixing a thermocouple precisely to the location of excited particles without interfering with the signal, a stainless-steel sheet was instead used for temperature calibration measurements. The phosphor luminescence intensity and emission spectrum dependence on temperature were measured using the setup in Figure 15. A Type K thermocouple was welded to the center of the stainless-steel sheet, and emission spectra were recorded at several temperatures by increasing the hot plate heating rate and waiting 15-25 minutes for the temperature to reach a steady value (less than 2 K/min drift). Prior to recording each spectrum, an image without any particle luminescence, a so-called "dark" image, was saved and later subtracted from the data image to isolate the intensity due to particle emission only. A 1-second integration time was applied to obtain high signal for recording data images, particularly at high temperatures when thermal quenching reduces the total emission intensity.

The normalized emission spectra during heating and cooling the plate illustrate the spectral broadening and blue-shift with increasing temperature (Figure 18). Except at long wavelengths where the emission signal decays close to zero, the collected spectra are found to be considerably less noisy than previous measurements due to improved positioning of the test article and focusing lens. UV interference from the filtered LDLS output (< 390 nm) was minimized by strategic positioning of the spectrometer to reduce UV reflection entering the lens.

To simulate the two-color intensity ratio calibration that will be applied for gas flow measurements, the transmission functions of two bandpass filters (Thorlabs FBH400-40 and FBH460-10) were used to digitally integrate against the measured spectra, and the simulated intensity ratios were plotted against temperature (Figure 19). A least-squares

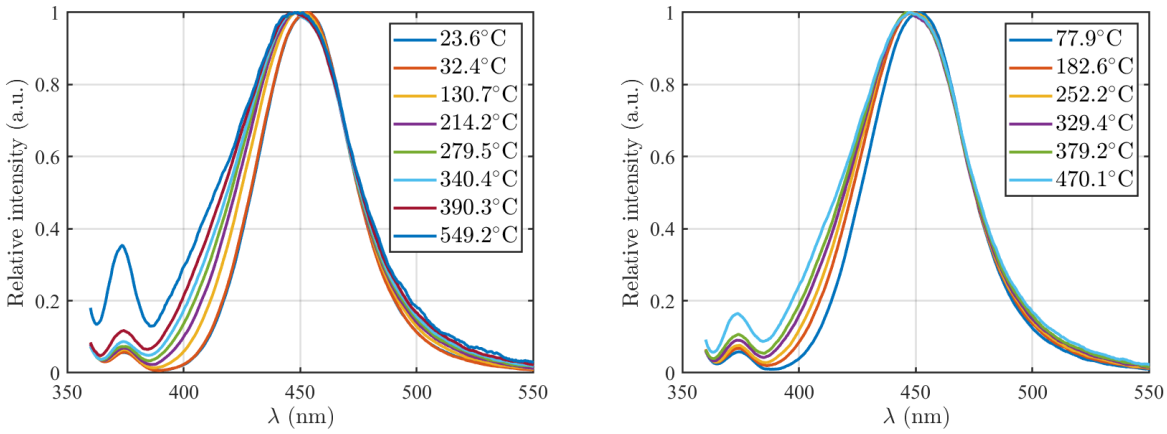

(a) Heating phase **(b)** Cooling phase

Figure 18: Normalized spectra collected during the heating and cooling phases of a horizontal stainless-steel plate on a hot plate.

quadratic fit was applied to the heating data, and the difference between predicted temperature using the calibration curve and the thermocouple measurement of each cooling data point was evaluated (Figure 19, right). There is a clear and consistent bias for the measured intensity ratio to predict a temperature substantially lower than the thermcouple reading, particularly at higher temperatures.

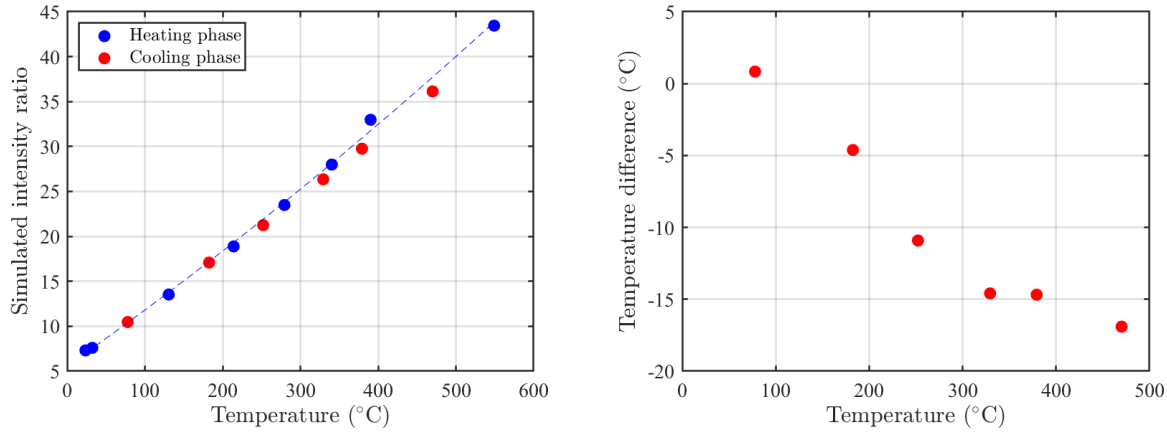

Figure 19: Simulated temperature calibration curve and out-of-sample measurement errors using example bandpass filters commonly employed for phosphor thermography.

The bias can be attributed in most part to thermal non-equilibrium between the thermocouple and phosphor particles. For the spectrometer to obtain sufficient signal for these measurements, the region of particle illumination had to be made larger than the thermocouple bead, which inevitably introduces a mismatch in the particle and thermocouple temperatures due to spatial temperature gradients. The direction of the bias further indicates a strong effect of thermal transients on the disparity in temperatures, which appears to widen at high temperatures when the magnitude of heating is larger and the temperature gradient between the heated surface and atmosphere becomes extremely sharp. The phosphor particles were placed on top of the thermocouple, so it is possible that convective heat transfer with the atmosphere led to lower predicted phosphor temperatures, as observed. Finally, it should be noted that the heating phase data

used for calibration are equally liable to be in error as the cooling data. Therefore, we must not ascribe the blue data and quadratic regression as ground truth. It is useful only to consider the difference in temperatures predicted by the heating and cooling phases rather than suggesting one data set is in error to the other.

4.2.2 266 nm excitation

To assess the feasibility of using an alternate excitation source for BAM:Eu^{2+} temperature calibration, a procedure similar to that described in Section 4.2.1 was performed using the 266 nm pulsed laser to compare the emission spectra and calibration curve to those obtained using the broadband UV excitation. A calibration curve was constructed for each excitation source (LDLS and 266 nm) using the filters 425-50 nm and 450-25 nm with 95% confidence intervals superposed to illustrate the distribution of new measurements (Figure 20). The most important conclusion from this investigation is the emission spectrum dependence on excitation spectrum, which shows that the excitation spectrum used in experiment must match that applied for calibration.

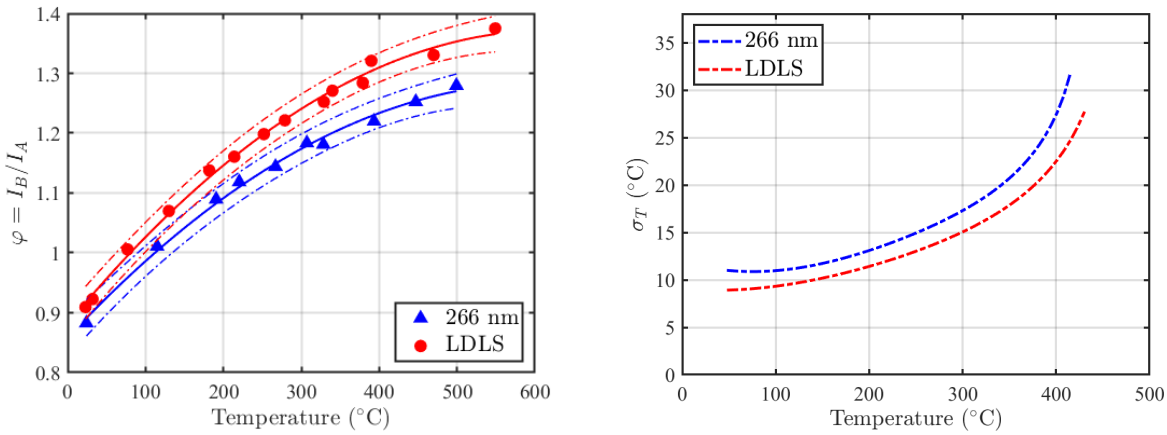

Figure 20: Comparison of the calibration curve generated using BAM:Eu^{2+} phosphor particles with different excitation spectra (left) and temperature measurement standard deviations (right).

4.3 Gas flow 2D intensity ratio measurements

The surface spectroscopy results served to verify the measurement principle and inform selection of bandpass filters for gas flow phosphor thermography. Initial testing was performed using the filter combination 400-50 nm (Edmund Optics #84-793) and 450-25 nm (Edmund Optics #86-665), but the 400-50 nm filter was found to attenuate the detected signal so greatly that the luminescence image differed little from the background image. This component was exchanged for a 425-50 nm filter (Edmund Optics #86-961), which captures approximately five times the integrated intensity at room temperature.

Examples of raw filtered luminescence images collected by the PCO cameras are given to provide a qualitative visualization of measured intensity and seeding concentration (Figure 21). Due to the small particle size, there exist large local intensity gradients that suggest the importance of excellent image alignment prior to pixelwise division for two-color intensity ratio temperature calibration. Alternatively, software binning has

been shown to reduce spatial variance of intensity ratio fields at the expense of spatial resolution.

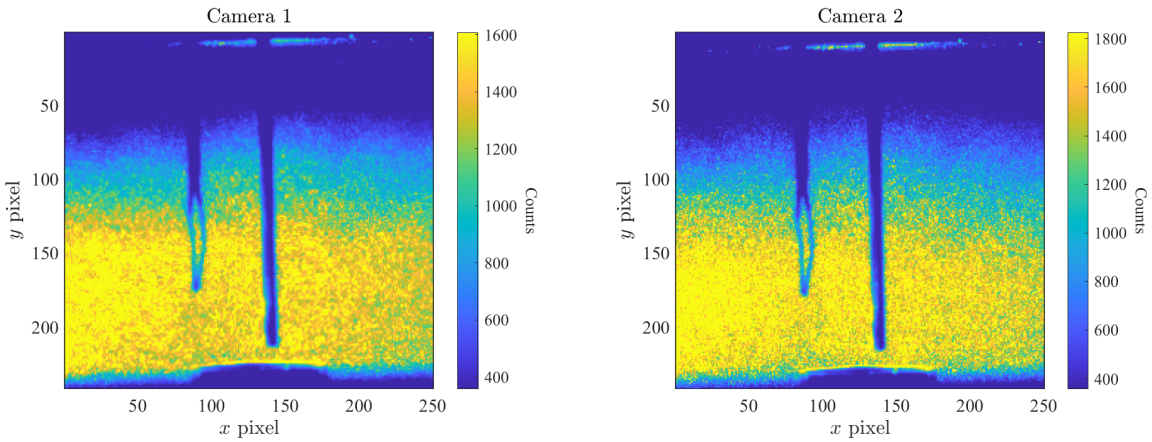

Figure 21: Luminescence intensity measured by PCO 2000 monochrome cameras with 425-50 nm (left) and 450-25 nm (right) bandpass filters.

Luminescence images were collected at several temperatures for decaying convection flows following particle suspension. The temperatures were recorded using a thermocouple suspended in the test volume, but this reading likely cannot be relied upon for an accurate calibration due to poor thermal contact between the thermocouple and fluid (air is a poor conductor), temporal transients especially during particle suspension, and high spatial gradients of emission intensity. In spite of this limitation preventing a full gas flow calibration, the raw intensity images were post-processed by performing background subtraction, cutoff filtering, 4×4 software binning, and image registration to compute intensity ratio fields (Figure 22). Note that intensity ratio field values outside the region of phosphor excitation, such as the jump in magnitude at the bottom of Figure 22 or the region masked by the thermocouple or copper tubing, cannot be relied upon for calibration or experimental temperature measurements due to their misrepresentation of the flow field and lack of luminescence signal. Despite the nonuniform particle seeding density and laser sheet profile (Figure 21), this spatial variance is not as pronounced in the intensity ratio fields (Figure 22), a promising result for future attempts at implementing gas flow phosphor thermography.

The change in intensity ratio due to the temperature increase is evident in the above figures. However, even with 4×4 software binning, the standard deviation of the field over the luminescence region is too large for a useful temperature calibration. For example, at 24 °C, the spatial mean intensity ratio is $\overline{\varphi} = 0.902$, and the standard deviation is $\sigma_\varphi = 0.122$. The intensity ratio standard deviation decreased for the 71 °C and 113 °C measurements but increased dramatically at higher temperatures due to decreasing signal from thermal quenching.

To obtain reliable calibration data for gas flow experiments, several challenges must be solved. First, there must be greater thermal contact between the temperature truth measurement device and the phosphor particles, which is accomplished by fixing thermocouples to a copper plate holding the particles. Next, the calibration will work best with higher particle density (without saturating the CCD sensor) because higher intensity reduces the intensity ratio uncertainty. Finally, accurate image alignment is critical to ensure the pixel-wise image division matches locations in physical space for intensity

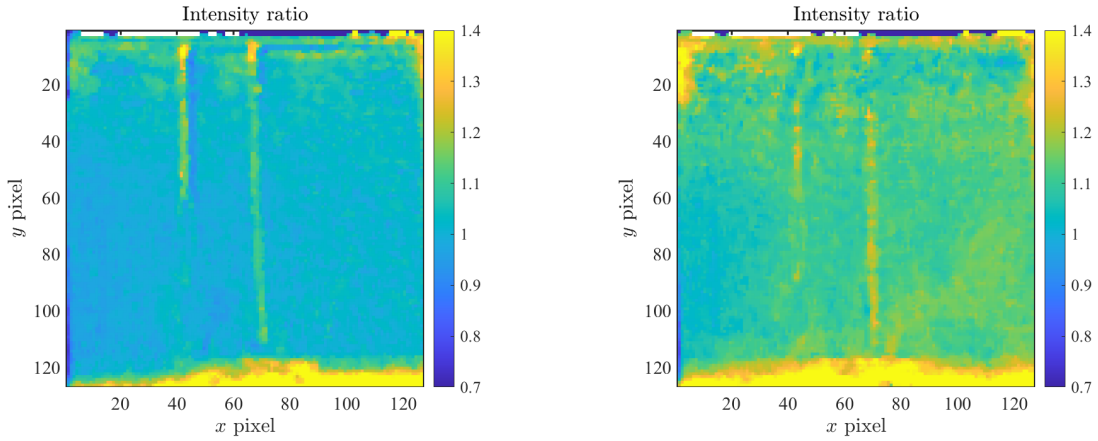

Figure 22: Intensity ratio fields for thermocouple readings 71 °C (left) and 113 °C (right). Note that these temperatures were not yet used for a full calibration due to limitations discussed in the text.

ratio calculation.

4.4 2D surface temperature calibration

The above improvements were implemented in a 2D surface temperature calibration to obtain the necessary data for measuring temperature using 266 nm excitation and PCO camera images. The inhomogeneous spatial distribution of particles in bulk powder form posed a challenge for obtaining quality results due to its effect on the spatial luminescence intensity variance, which caused some CCD pixels to receive no light and others to become saturated. To overcome this challenge, BAM:Eu^{2+} particles were adhered to a copper plate (5 cm × 5 cm) by dissolving the particles in water, painting the solution on the surface using a brush, and heating the plate to $30-40$ °C to evaporate the liquid, leaving behind a thin coat of particles. Although there was visible nonuniformity in the resulting film, the particle mass distribution was a significant improvement over the bulk powder approach and prevented the particles from moving during calibration data collection.

Four thermocouples were fixed around the perimeter of the copper plate using screws, and the thermocouples were insulated to ensure contact with the copper only (Figure 23). After depositing the phosphor film, the plate was placed on a hot plate, and alignment images were captured to perform control point image registration using features visible from ambient room lighting. Thirty offset frames (with no particle excitation or extraneous light) were collected. Intensity fields were captured by the two PCO cameras at seven temperatures ranging from 22 °C to 422 °C. Temperature data were collected at 1 Hz over 30 seconds to verify low temporal temperature variance at the time of intensity ratio field capture. The mean of the four thermocouple time-series means,

$$\overline{T} = \frac{1}{4}\sum_{i=1}^{4}\frac{1}{30}\sum_{k=1}^{30}T_i(t_k), \tag{9}$$

was used as the temperature of each calibration point.

The steps of image post-processing used to convert each pair of intensity fields to intensity ratio fields were (1) offset subtraction, (2) image registration, (3) software binning, and (4) image division. A region of interest $\mathcal{A}$ containing n pixels was established

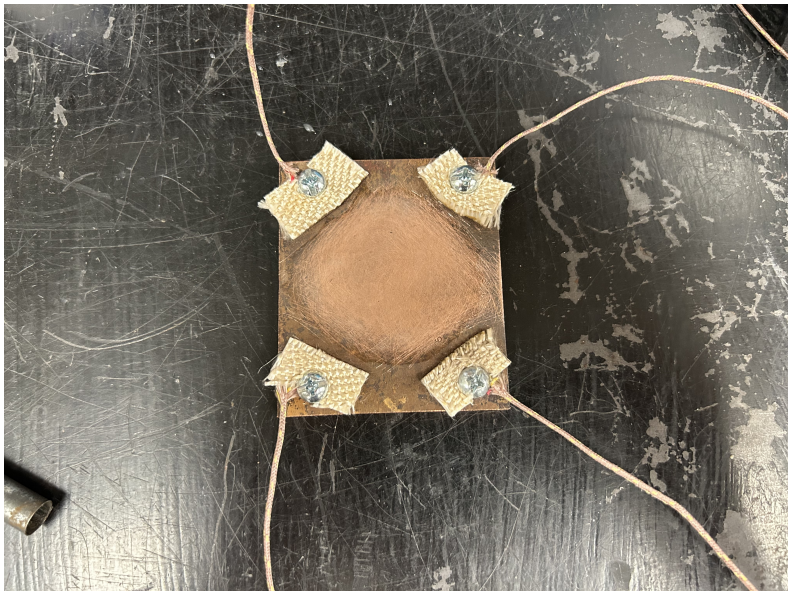

Figure 23: Copper plate with thermocouples attached prior to surface deposition of phosphor particles.

by manually selecting illuminated points inside a user-specified polygon. At each time t_k, a spatial average intensity ratio was computed by

$$\overline{\varphi}_k(T) = \frac{1}{n} \sum_{\{(i,j)\in\mathcal{A}\}} \varphi_{i,j,k}(T), \tag{10}$$

where $\varphi_{i,j,k}$ denotes the intensity ratio at pixel (i, j) at time t_k. The spatial standard deviation of each image pair's intensity ratio was computed at each time by

$$\widehat{\sigma}_{\varphi_k}(T) = \sqrt{\frac{1}{n-1} \sum_{\{(i,j)\in\mathcal{A}\}} (\varphi_{i,j,k}(T) - \overline{\varphi}_k(T))^2}. \tag{11}$$

Time-series plots of spatial mean and standard deviation of the intensity ratio are given for all tested temperatures using 2×2 and 4×4 software binning in Figures 24 and 25, respectively. These results illustrate that increasing the number of binned pixels does not change the mean measured intensity ratio but reduces the time-average of spatial standard deviation.

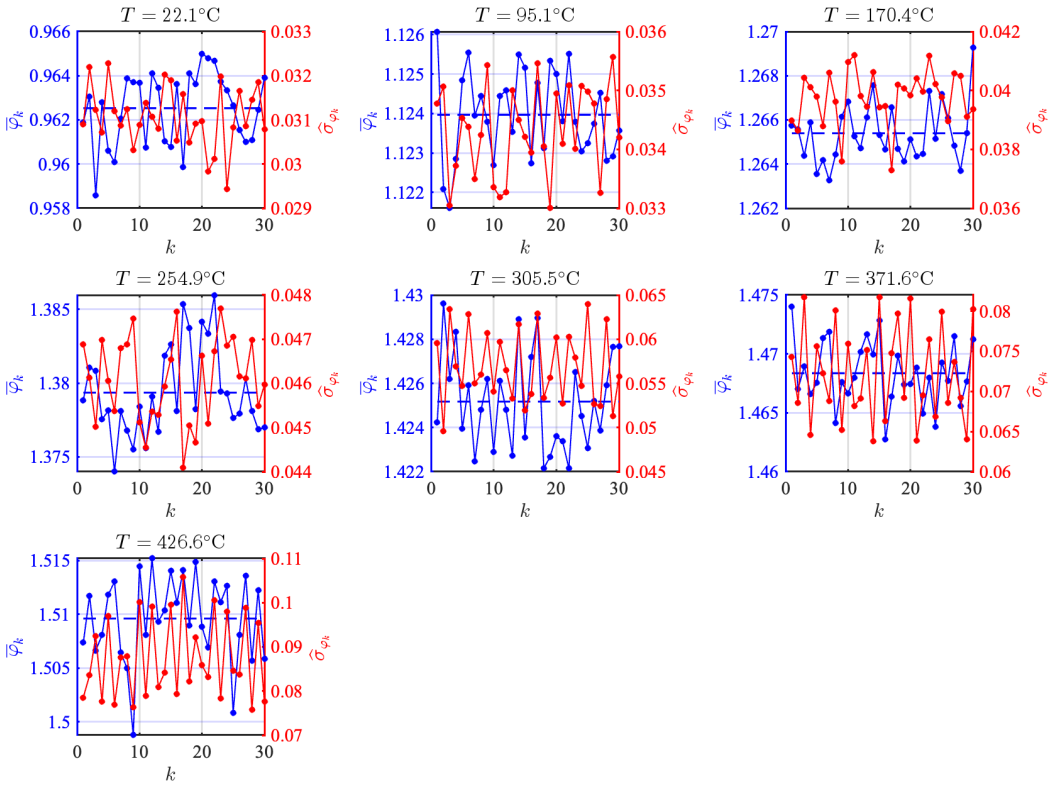

Figure 24: Time-series intensity ratio spatial mean and standard deviation over thirty frames at seven calibration temperatures using 2×2 software binning.

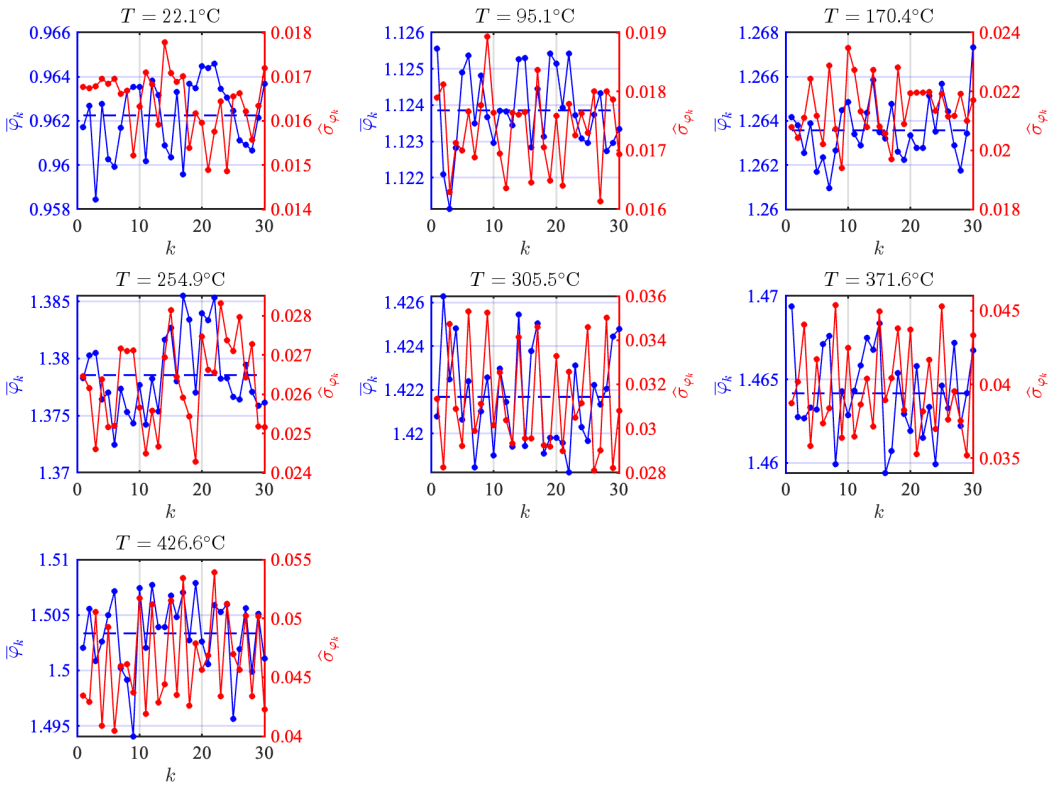

Figure 25: Time-series intensity ratio spatial mean and standard deviation over thirty frames at seven calibration temperatures using 4×4 software binning.

The temporal mean and standard deviation of these spatial quantities were computed according to

$$\overline{\varphi}(T) = \frac{1}{n_T} \sum_{k=1}^{n_T} \overline{\varphi}_k(T) \tag{12}$$

and

$$\widehat{\sigma}_{\varphi}(T) = \frac{1}{n_T} \sum_{k=1}^{n_T} \widehat{\sigma}_{\varphi_k}(T), \tag{13}$$

where n_T denotes the number of frames used to compute the time-averaged statistics. These estimates $\overline{\varphi}(T)$ and $\widehat{\sigma}_{\varphi}(T)$ were used to construct a calibration curve with $\pm 1\sigma$ bounds. Two calibration curves were constructed, one using 2×2 software binning and the other using 4×4 software binning (Figure 26).

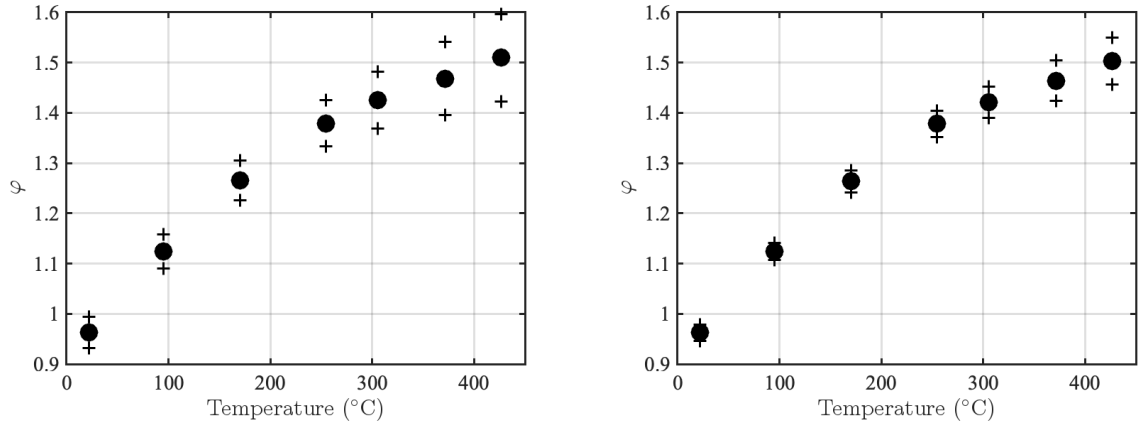

Figure 26: Calibration curves using spatial mean intensity ratio and $\pm 1\sigma$ bounds with 2×2 (left) and 4×4 (right) software binning.

Several lessons were learned throughout the process of obtaining and post-processing data for 2D temperature calibration. First, the image alignment was found to be of paramount importance in obtaining low-variance intensity ratio fields, especially in preliminary experiments with nonuniform phosphor particle density and thus high intensity gradients. This was less important for the particle film created by the dissolution and evaporation technique, which promoted more uniform particle density, but still critical due to the nonuniform excitation laser profile. Next, one limitation of the present filter combination evident in the calibration curves is the simultaneous increase in spatial variance σ_{φ} and decrease in fractional sensitivity φ'/φ, as well as the decrease in overall luminescence intensity arising due to thermal quenching. These effects compound to drastically increase the temperature measurement uncertainty given in Equation 7. Consequently, a new filter combination with a more linear calibration curve profile may be necessary for future experiments at higher temperatures ($T > 300\,^{\circ}\mathrm{C}$). Lastly, the calibration temperature "ground truth" used to construct the curves in Figure 26 were based on the temporal mean of four thermocouples surrounding the particles, so there are multiple sources of unaccounted error in the temperature measurements that should be considered in a more detailed statistical analysis of the calibration results.

5 Conclusions and future work

In this project, an experiment was designed to obtain simultaneous velocity and temperature measurements inside a gas mixture using TPIV. Phosphor particles were selected based on a target temperature range for measuring thermal ignition. The experimental setup consisted of a dual-cavity pulsed laser, a second harmonic generator, sheet-forming lenses, a test section, and scattering and luminescence detectors.

PIV was performed using BAM:Eu^{2+} phosphor particles, which have a $\sim$10X smaller median diameter than the oil droplets used in previous studies. This investigation found that a higher magnification is required for BAM:Eu^{2+} than oil particles due to size and lower scattering efficiency. This poses a fundamental limit on the physical field-of-view achievable with the present setup for a fixed CMOS sensor resolution.

Two-color thermography using BAM:Eu^{2+} with continuous, broadband excitation and single-line excitation (266 nm) was applied to generate temperature calibration curves and their associated 95% confidence intervals for out-of-sample measurements over the temperature range $20-550\,^{\circ}\mathrm{C}$. The calibration curves were found to have non-overlapping 95% confidence intervals above $160\,^{\circ}\mathrm{C}$ with the gap widening at higher temperature. This proves the importance of using the same excitation spectrum in calibration and experiment.

In-situ gas flow calibration has yet to be successful due to challenges associated with large temperature gradients in the test volume, thermal non-equilibrium between the air and thermocouple, and lack of luminescence intensity as the particles settle following impulsive suspension. However, a successful 2D surface calibration using 266 nm excitation motivates continued work on gas flow calibration by developing a more accurate system for measuring temperature ground truth. An in-situ calibration will provide data to convert gas flow intensity ratio images into full temperature fields, enabling visualization of a combustible mixture prior to ignition.

6 Acknowledgements

This work was funded by The Boeing Company through Strategic Research and Development Relationship Agreement CT-BA-GTA-1. I wish to thank my mentors Joseph Shepherd and Charline Fouchier for their guidance and support throughout the project. This experience would not have been possible without the generous contribution from the Fred and Jean Felberg SURF Fellow donors.

7 References

[1] ASTM International. ASTM E659-15, Standard Test Method for Autoignition Temperature of Liquid Chemicals. Standard, 2015.

[2] Conor D Martin and Joseph E Shepherd. Low temperature autoignition of Jet A and surrogate jet fuel. *Journal of Loss Prevention in the Process Industries*, 71:104454, 2021.

[3] Markus Raffel, Christian E Willert, Fulvio Scarano, Christian J Kähler, Steve T Wereley, and Jürgen Kompenhans. *Particle image velocimetry: a practical guide*. Springer, 2018.

[4] Cameron Tropea, Alexander L Yarin, John F Foss, et al. *Springer handbook of experimental fluid mechanics*, volume 1. Springer, 2007.

[5] William Thielicke and Eize J. Stamhuis. PIVlab – Towards User-friendly, Affordable and Accurate Digital Particle Image Velocimetry in MATLAB. *Journal of Open Research Software*, 2, October 2014.

[6] William Thielicke. *The flapping flight of birds: analysis and application*. Uitgever niet vastgesteld, Nederland, 2014. OCLC: 892847727.

[7] William Thielicke and René Sonntag. Particle image velocimetry for MATLAB: Accuracy and enhanced algorithms in PIVlab. *Journal of Open Research Software*, 9, 2021.

[8] Dustin Witkowski. *Investigation of thermographic phosphors for gas-phase temperature measurements in combustion applications*. The University of Wisconsin-Madison, 2017.

[9] Ryo Hasegawa, Ichiro Sakata, Hiromichi Yanagihara, Gustaf Särner, Mattias Richter, Marcus Aldén, and Bengt Johansson. Two-dimensional temperature measurements in engine combustion using phosphor thermometry. *SAE Transactions*, pages 405–411, 2007.

[10] Alaa Omrane, Greger Juhlin, Frederik Ossler, and Marcus Aldén. Temperature measurements of single droplets by use of laser-induced phosphorescence. *Applied optics*, 43(17):3523–3529, 2004.

[11] Dustin Witkowski, David A Rothamer, Amy Lynch, and Vince Belovich. Measurements of the temperature and velocity fields in a free shear flow between a vitiated stream and clean air stream using a Pr:YAG thermographic phosphor. *Measurements*, pages 070DI–00321, 2013.

[12] J Brübach, A Patt, and A Dreizler. Spray thermometry using thermographic phosphors. *Applied Physics B*, 83:499–502, 2006.

[13] Christopher Abram, Benoît Fond, and Frank Beyrau. Temperature measurement techniques for gas and liquid flows using thermographic phosphor tracer particles. *Progress in energy and combustion science*, 64:93–156, 2018.

[14] Christopher Abram, Benoit Fond, Andrew L Heyes, and Frank Beyrau. High-speed planar thermometry and velocimetry using thermographic phosphor particles. *Applied Physics B*, 111:155–160, 2013.

[15] Benoit Fond, Christopher Abram, and Frank Beyrau. Characterisation of the luminescence properties of BAM:Eu2+ particles as a tracer for thermographic particle image velocimetry. *Applied Physics B*, 121(4):495–509, December 2015.

[16] Gustaf Särner, Mattias Richter, and Marcus Aldén. Investigations of blue emitting phosphors for thermometry. *Measurement Science and Technology*, 19(12):125304, December 2008.

[17] Benoit Fond, Christopher Abram, Andrew L Heyes, Andreas M Kempf, and Frank Beyrau. Simultaneous temperature, mixture fraction and velocity imaging in turbulent flows using thermographic phosphor tracer particles. *Optics Express*, 20(20):22118, September 2012.

[18] Dustin Witkowski, Joshua M. Herzog, and David A. Rothamer. Combustion-relevant temperature imaging with scattering referenced aerosol phosphor thermometry applied to Eu:BAM. *Combustion and Flame*, 224:233–238, February 2021.

[19] S. Allison, D. Beshears, T. Bencic, W. Hollerman, and P. Boudreaux. Development of temperature-sensitive paints for high-temperature aeropropulsion applications. In *37th Joint Propulsion Conference and Exhibit*, Salt Lake City,UT,U.S.A., July 2001. American Institute of Aeronautics and Astronautics.

[20] Dustin Witkowski and David A. Rothamer. Investigation of aerosol phosphor thermometry (APT) measurement biases for Eu:BAM. *Applied Physics B*, 124(10):202, October 2018.

[21] Hyunchang Lee, Benjamin Böhm, Amsini Sadiki, and Andreas Dreizler. Turbulent heat flux measurement in a non-reacting round jet, using BAM:Eu2+ phosphor thermography and particle image velocimetry. *Applied Physics B*, 122(7):209, July 2016.

[22] Joshua M. Herzog, Dustin Witkowski, and David A. Rothamer. Combined scattering-referenced and co-doped aerosol phosphor thermometry using the Ce,Pr:LuAG phosphor. *Applied Physics B*, 127(7):103, July 2021.

[23] Dustin Witkowski. *Investigation of Thermographic Phosphors for Gas-Phase Temperature Measurements in Combustion Applications*. PhD thesis, The University of Wisconsin-Madison, January 2017. Publication Title: Ph.D. Thesis ADS Bibcode: 2017PhDT.....64W.

[24] P. Schreivogel, C. Abram, B. Fond, M. Straußwald, F. Beyrau, and M. Pfitzner. Simultaneous kHz-rate temperature and velocity field measurements in the flow emanating from angled and trenched film cooling holes. *International Journal of Heat and Mass Transfer*, 103:390–400, December 2016.

[25] Marcus Aldén, Alaa Omrane, Mattias Richter, and Gustaf Särner. Thermographic phosphors for thermometry: A survey of combustion applications. *Progress in Energy and Combustion Science*, 37(4):422–461, August 2011.

[26] Dustin Witkowski, David A Rothamer, Amy Lynch, and Vince Belovich. Measurements of the Temperature and Velocity Fields in a Free Shear Flow between a Vitiated Stream and Clean Air Stream using a Pr:YAG Thermographic Phosphor. *Measurements*, 2013.

[27] Dustin Witkowski and David A. Rothamer. Emission properties and temperature quenching mechanisms of rare-earth elements doped in garnet hosts. *Journal of Luminescence*, 192:1250–1263, December 2017.

[28] Dustin Witkowski and David A. Rothamer. Precise surface temperature measurements from 400 to 1200 K using the Pr:YAG phosphor. *Applied Physics B*, 127(12):171, December 2021.

[29] Jonathan Jordan and David A. Rothamer. Pr:YAG temperature imaging in gas-phase flows. *Applied Physics B*, 110(3):285–291, March 2013.

[30] Dustin Witkowski and David A Rothamer. Scattering referenced aerosol phosphor thermometry. *Measurement Science and Technology*, 30(4):044003, April 2019.

[31] Dustin Witkowski and David A. Rothamer. A novel strategy to improve the sensitivity of aerosol phosphor thermometry using co-doped phosphors. *Proceedings of the Combustion Institute*, 37(2):1393–1400, 2019.

[32] Rongfeng Guan, Liu Cao, Yajun You, and Yuebin Cao. The Luminescence Properties and Energy Transfer from Ce $^{3+}$ to Pr $^{3+}$ for YAG:Ce $^{3+}$ Pr $^{3+}$ Phosphors. *Journal of Nanomaterials*, 2015:1–8, 2015.

[33] Joshua M. Herzog, Dustin Witkowski, and David A. Rothamer. Combustion-relevant aerosol phosphor thermometry imaging using Ce,Pr:LuAG, Ce:GdPO4, and Ce:CSSO. *Proceedings of the Combustion Institute*, 38(1):1617–1625, 2021.

[34] Joshua M. Herzog, Dustin Witkowski, and David A. Rothamer. Characterization of the Ce,Pr:LuAG phosphor for Co-doped aerosol phosphor thermometry. *Journal of Luminescence*, 229:117665, January 2021.

[35] Dustin Witkowski and David A. Rothamer. A methodology for identifying thermographic phosphors suitable for high-temperature gas thermometry: application to Ce3+ and Pr3+ doped oxide hosts. *Applied Physics B*, 123(8):226, August 2017.

[36] Joshua M Herzog, Dustin Witkowski, and David A Rothamer. Characterization of Ce:CSSO, Pr:CSSO, and co-doped Ce,Pr:CSSO phosphors for aerosol phosphor thermometry. *Measurement Science and Technology*, 32(5):054008, May 2021.

[37] Christopher Abram, Benoit Fond, and Frank Beyrau. High-precision flow temperature imaging using ZnO thermographic phosphor tracer particles. *Optics Express*, 23(15):19453, July 2015.

[38] Christopher Abram, Benoît Fond, and Frank Beyrau. Temperature measurement techniques for gas and liquid flows using thermographic phosphor tracer particles. *Progress in Energy and Combustion Science*, 64:93–156, January 2018.